arXiv:0905.0446v1 [quant-ph] 4 May 2009

# Ultra-Broadband Coherence-Domain Imaging Using Parametric Downconversion and Superconducting Single-Photon Detectors at 1064 nm

Nishant Mohan,[1,*] Olga Minaeva,[2,3] Gregory N. Goltsman,[3] Mohammed F. Saleh,[2] Magued B. Nasr,[2] Alexander V. Sergienko,[2,4] Bahaa E. A. Saleh,[2,5] and Malvin C. Teich[1,2,4]

[1] *Department of Biomedical Engineering, Boston University, Boston MA 02215*

[2] *Department of Electrical and Computer Engineering, Boston University, Boston MA 02215*

[3] *Department of Physics, Moscow State Pedagogical University, Moscow 119992, Russia*

[4] *Department of Physics, Boston University, Boston MA 02215*

[5] *College of Optics and Photonics (CREOL), University of Central Florida, Orlando FL 32816*

[*] *Corresponding author: nm82@bu.edu*

Coherence-domain imaging systems can be operated in a single-photon counting mode, offering low detector noise; this in turn leads to increased sensitivity for weak light sources and weakly reflecting samples. We have demonstrated that excellent axial resolution can be obtained in a photon-counting coherence-domain imaging (CDI) system that uses light generated via spontaneous parametric down-conversion (SPDC) in a chirped periodically poled stoichiometric lithium tantalate (chirped-PPSLT) structure, in conjunction with a niobium nitride superconducting single-photon detector (SSPD). The bandwidth of the light generated via SPDC, as well as the bandwidth over which the SSPD is sensitive, can extend over a wavelength region that stretches from 700 to 1500 nm. This ultra-broad wavelength band offers a near-ideal combination of deep penetration and ultra-high axial resolution for the imaging of biological tissue. The generation of SPDC light of adjustable bandwidth in the vicinity of 1064 nm, via the use of chirped-PPSLT structures, had not been previously achieved. To demonstrate the usefulness of this technique, we have constructed images for a hierarchy of samples of increasing complexity: a mirror, a nitrocellulose membrane, and a biological sample comprising onion-skin cells. © 2009 Optical Society of America

*OCIS codes:* 110.4500, 190.4975, 040.5160.

## 1. Introduction

Over the past decade, coherence-domain imaging (CDI), particularly optical coherence tomography (OCT), has come into its own. OCT relies on the interference of partially coherent light to achieve axial sectioning [1]. The technique has been highly successful, particularly in biology and medicine [2–4]. Indeed, in recent years, OCT has joined the armamentarium of diagnostic imaging techniques, and has found use in clinical ophthalmology [5], dermatology [6], cardiology [7], and gastroenterology [8]. In biological tissue, OCT typically achieves an axial resolution of a few $\mu$m and achieves imaging to depths of 2–3 mm [9].

The central wavelength at which a biological CDI system operates is an important parameter; optical scattering in biological tissue makes it difficult to image deeply in the visible region so that most CDI systems make use of light sources with wavelengths longer than 700 nm. The limitation on the long-wavelength side is governed by the absorption of water, which becomes substantial at about 1500 nm. Moreover, since the axial resolution of a CDI system improves as the spectral bandwidth of the light source increases, use of the entire wavelength range from 700 to 1500 nm provides a suitable combination of deep penetration and ultra-high resolution for biological tissue [10].

In this paper, we demonstrate that coherence-domain imaging may be achieved at a low photon-flux level by making use of light generated by spontaneous parametric down-conversion (SPDC) in a chirped periodically poled stoichiometric lithium tantalate (chirped-PPSLT) structure, via phase matching to the fundamental. This structure is pumped with 532-nm CW light from a high-power laser to generate broadband light centered at 1064 nm. Broadband SPDC has been generated previously in chirped periodically poled structures, but only in the 800-nm region and only via phase matching to the third harmonic, which is less efficient [11–14]. We have built on our previous efforts [10] in carrying out photon-counting optical coherence-domain reflectometry with superconducting single-photon detectors (SSPDs), which are sensitive over the entire spectral range of interest for biological imaging, namely 700–1500 nm.

Section II summarizes the theory of the SPDC optical source, along with optical spectra calculated for parameter ranges of interest. This is followed in Sec. III by the experimental spectra obtained from the chirped structure, as well as the results of photon-counting CDI experiments that make use of this source. In particular, we display CDI interferograms for a hierarchy of samples of increasing complexity: a mirror, a pellicle, and a biological sample comprising onion-skin tissue. In the discussion provided in Sec. IV, we compare the relative merits of using the chirped-PPSLT SPDC source and SSPD detector for CDI with other more conventional sources and detectors.

## 2. Design of Downconversion Source

Consider the process of SPDC in which a pump wave at frequency $\omega_p$ is down converted to signal and idler waves at frequencies $\omega_s$ and $\omega_i$, respectively, such that $\omega_p = \omega_s + \omega_i$. The power spectral density $S(\omega_s)$ of the downconverted light (signal or idler) is governed by the phase-matching condition in the nonlinear structure, which, for collinear emission is given by [1]

$$S(\omega_s) \propto \left| \int_0^L d(z)\, \exp[-j\, \Delta k(\omega_s)\, z]\, dz \right|^2 , \tag{1}$$

where $z$ is the distance along the direction of propagation of the waves, $L$ is the overall length of the structure, $d$ is the effective second-order nonlinear coefficient of the material, and $\Delta k$ is the phase mismatch between the pump and the downconverted waves.

Both the local period of the nonlinear coefficient $d(z)$ and $\Delta k$ depend on temperature $T$, so that the power spectral density is also a function of temperature. The dependence of $\Delta k$ on the signal frequency and temperature is provided by

$$\Delta k(\omega_s) = \frac{n(\omega_p\,, T)\omega_p}{c} - \frac{n(\omega_s\,, T)\omega_s}{c} - \frac{n(\omega_p - \omega_s\,, T)(\omega_p - \omega_s)}{c}\,, \tag{2}$$

where $c$ is the speed of light in vacuum and $n$ is the refractive index of the material; its dependence on frequency and temperature can be determined from the temperature-dependent

Sellemeier equation [15].

The function $d(z)$ in Eq. (1) for a structure with chirped poling is given by

$$d(z) = \sum_{k=1}^{N} s(z - a_k, b_k), \tag{3}$$

where $N$ is the total number of periods. The quantity $b_k$ in Eq. (3) represents the width of the $k$th period. For a bipolar rectangular pulse, $s(z, b)$ is given by

$$s(z,b) = \begin{cases} 1, & 0 < z \leq b/2 \\ -1, & b/2 < z \leq b \\ 0, & \text{otherwise.} \end{cases} \tag{4}$$

For a crystal poled with a linearly chirped spatial frequency, $b_k$ is given by $1/b_k = 1/b_1 - (k-1)\zeta$, where $\zeta$ is the chirp parameter. The term $a_k$ in Eq. (3) represents the starting location of the $k$th period and is represented by the iterative relation $a_k = a_{k-1} + b_{k-1}$ with $a_1 = 0$. The features of the structure, i.e., $b_k$ for $1 < k \leq N$, is defined entirely by the length of the first period $b_1$ and the chirp parameter $\zeta$.

Our calculations were carried out for stoichiometric lithium tantalate (SLT) as the nonlinear optical material. The parameters used for the calculations were the same as those of the actual structures used in our experiments, which we report in Sec. 3.B. The actual poling was conducted in such a way that three separate structures were fabricated on the same substrate, enabling us to carry out measurements for structures with different chirp parameters; this also enabled us to better judge the validity of our theory. The three structures have just about the same overall length ($L \approx 2$ cm) and number of periods ($N \approx 2515$), but different chirp parameters $\zeta$ and lengths of the first period $b_1$. The first of the three structures has $b_1 = 7.95\,\mu$m and $\zeta = 0$, i.e., it is unchirped. The second has $b_1 = 7.85\,\mu$m and $\zeta = 1.26 \times 10^{-6}\,\mu\text{m}^{-1}$, whereas the third structure has the highest chirp with $b_1 = 7.5\,\mu$m and $\zeta = 6.24 \times 10^{-6}\,\mu\text{m}^{-1}$. For SLT, the temperature dependence of the width of each period can be accommodated via the relation: $b_k(T) = b_k(25)\,[\alpha(T-25) + \beta(T-25)^2]$, where $\alpha$ and $\beta$ are thermal expansion coefficients and $T$ is the temperature in degrees Celsius [15].

The parameters $b_1$ and $\zeta$ enable us to determine $d(z)$ while the temperature-dependent Sellmeier equation, along with the pump frequency $\omega_p = 5.6 \times 10^{14}$ Hz (corresponding to a pump wavelength of 532 nm), provides us with $\Delta k$. Inserting $d(z)$ and $\Delta k$ in Eq. (1) enables us to obtain the estimated power spectral density of the output signal beam for different temperatures, via numerical evaluation. The wavelength ranges of spectral components that are present, at various temperatures, are displayed as brightness images in Fig. 1 for the unchirped structure [Fig. 1(a)], the medium-chirped structure [Fig. 1(b)], and the maximum-chirped structure [Fig. 1(c)]. The calculated normalized spectrum is displayed in Fig. 1(d) for the maximum-chirped structure at a temperature of 80° C.

## 3. Experiments

### *3.A. Generic experimental arrangement*

The generic interferometric arrangement for the experiments we report in this Section is schematized in Fig. 2(a). The experiments were carried out using either single-mode-fiber-coupled downconversion or single-mode-fiber-coupled light from a superluminescent diode (SLD). The broadband light emanating from the source was coupled into a single-mode (SM) fiber and collimated by lens L3 before being fed into the Michelson interferometer. The light in the interferometer was focused onto the reference mirror and the sample using lenses L4 and L5, respectively. Lens L4 and the reference mirror were placed on a single nanopositioning stage while the sample was placed on another one. Their positions were changed in accordance with the arrows shown in the figure. The light exiting the interferometer was fed into either a single-photon avalanche detector (SPAD) or a SSPD via fiber-coupling and a lens (not shown). It is worth noting that the optical components should be transmissive over a broad band of wavelengths when working with broadband optical imaging systems.

The downconversion source, shown in Fig. 2(b), consisted of light from a cw frequency-doubled $Nd^{3+}$:$YVO_4$ laser (Coherent Verdi), operating at a wavelength of 532 nm and at a power of 2 W, that pumped a chirped-PPSLT device with three separate structures fabricated on the same substrate, as described previously. The structure was aligned to obtain collinear SPDC. The downconverted light was collimated using a lens (L1) and coupled into a SM fiber via another lens (L2). The filter, comprising a dichroic mirror and a longpass filter, served to remove the pump and to allow only the downconverted light to be coupled into the fiber. The light from the SLD (Superlum SLD-47-MP) was centered at a wavelength of 930 nm and had a full-width at half-maximum (FWHM) spectral width of 70 nm.

Optical imaging systems often make use of commercially available Si or InGaAs semiconductor detectors, depending on the wavelength at which the system operates. Roughly speaking, Si photodiodes are used for wavelengths shorter than 1100 nm and operate best in the vicinity of 800 nm, whereas InGaAs photodiodes, which are designed for operation in the vicinity of 1300 nm, are used for wavelengths longer than 1100 nm. The Si SPADs used in our experiments are incorporated in commercially available single-photon counting modules (Perkin-Elmer, Model SPCM-AQR-15-FC).

Inasmuch as neither Si nor InGaAs are sensitive over the entire spectral range of 700–1500 nm, however, we have followed our previous work and assayed the use of SSPDs in photon-counting optical coherence-domain imaging [10]. Such detectors offer some benefits for single-photon-counting applications, especially in the infrared, since they exhibit low dark-count rates and operate in a spectral region that stretches from 0.4 to 6 $\mu$m [16], which includes the region of biological interest. The SSPDs used were fabricated from 4-nm-thick superconducting niobium nitride (NbN) films [17]; their operation has been described else-

where [10, 18]. The quantum efficiency monotonically decreases with increasing wavelength of the incident light. Measurements using SSPDs were carried out in the same way as those described previously [10].

### *3.B. Observed downconversion spectra for different chirp parameters*

In this set of experiments, we measured the spectra associated with the downconverted light emitted by the three different chirped-PPSLT structures, as a function of temperature. The parameters for these structures were provided in Sec. 2, where the calculated spectra were reported (see Fig. 1). The experiments were carried out using the setup displayed in Fig. 2, which makes use of SM-fiber-coupled downconversion as the source, a SSPD as the detector, and a mirror as the sample. The counts from the SSPD were measured in a fixed time window, as a function of the reference-arm displacement (position of the reference mirror). The resultant interferograms were Fourier-transformed to obtain an estimate of the power spectral density of the downconverted light from the structures at different temperatures.

The experimental results are displayed as brightness images for the unchirped, medium-chirped, and maximum-chirped structures in Figs. 3(a), (b), and (c), respectively. The observed normalized spectrum is displayed in Fig. 3(d) for the maximum-chirped structure at a temperature of 80° C.

The spectral content of downconversion from the three chirped-PPSLT structures, which are stable and predictable, roughly follow the calculated patterns (see Fig. 1). For the unchirped structure, the phase matching is satisfied for two narrow bands of wavelengths. The widths of these bands increase for the medium-chirped structure, and a broad wavelength band emerges for the maximum-chirped structure. The spectra obtained for the unchirped and medium-chirped structures are slightly broader than those predicted by the calculations. We attribute this to the presence of the collimating lens (L1), which collects the downconverted beams over a finite angular range, rather than collinearly. Also, the measured optical power at longer wavelengths is smaller than that expected on the basis of the calculations. We believe that this arises because of a reduction in the quantum efficiency of the SSPD, as well as changes in the transmittance of the optical components, as the wavelength increases.

These results illustrate that we have a sound understanding of the features of SPDC light generation via chirped-PPSLT structures, thereby allowing us to engineer broadband spectra as desired.

### *3.C. Axial resolution for coherence-domain imaging with different sources and detectors*

We next carried out a set of experiments to determine the relative merits of using different sources of light and different detectors for coherence-domain imaging.

After examining the axial resolution achievable by using broadband SPDC (from the struc-

ture with the greatest chirp at a temperature of 80° C; see Sec. 3.B) in conjunction with a SSPD, we demonstrate that the resolution is diminished when the SSPD is replaced by a SPAD. We then proceed to show that the resolution is further diminished when the downconversion source is replaced by a SLD.

The axial resolution is determined by examining the widths of the interferogram envelopes using a mirror as the sample, as well as by making use of a pellicle as the sample.

In the first set of experiments to measure the axial resolution, we used a mirror as the sample in the experimental arrangement depicted in Fig. 2. We constructed interferograms by measuring the counts from the detector in a fixed time window, as a function of the position of the reference mirror (see Sec. 3.B), using the three source/detector combinations indicated above. The results are illustrated in Fig. 4. They reveal that the FWHM of the interferogram envelopes increase from 1.6 to 2.8 to 6.3 $\mu$m for the SPDC/SSPD, SPDC/SPAD, and SLD/SSPD combinations, respectively. Since the narrower the width of the envelope, the better the resolution, this demonstrates that the downconverted light with a superconducting detector yielded the highest resolution of the three source/detector combinations considered.

Another way of measuring the resolving power of an optical system is to test its ability to distinguish reflections from two nearby surfaces. The second set of experiments was similar to the first set, as described above, except that we replaced the mirror by a pellicle in the experimental arrangement depicted in Fig. 2. The pellicle was a nitrocellulose membrane (Thorlabs) of refractive index $n = 1.5$ and thickness $L = 2\,\mu$m.

Again we constructed interferograms using the three source/detector combinations indicated above. The results are illustrated in Fig. 5. It is evident that only the combination of a broadband downconversion source and a superconducting detector (Fig. 5(a)) was capable of clearly resolving the two surfaces of the membrane, indicating that this combination offered the highest resolution. The measured optical path length between the reflections is seen to be 3 $\mu$m in Fig. 5(a); this corresponds to a physical distance of $3/n = 2\,\mu$m, which nicely matches the thickness of the pellicle.

In terms of resolution, then, these experiments lead us to conclude that, in the vicinity of 1064 nm and of the source/detector combinations we examined, the optimal combination for coherence-domain imaging comprises broadband downconverted light with a superconducting detector.

### *3.D. Coherence-domain imaging of a biological sample*

Finally, we demonstrated the photon-counting coherence-domain imaging of a biological sample, comparing the performance of two source/detector combinations.

The sample was an onion-skin tissue from a white onion that was adhered to a cover slip

using a small drop of water. The sample was placed in the generic experimental setup depicted in Fig. 2 and a collection of A-scans were obtained at different transverse ($x$) positions along the sample. At a given transverse position, the lens–mirror combination (L4 and reference mirror) was scanned in the $z$ direction over a range of 70 $\mu$m, using a step size of 100 nm, and counts were recorded at each step for a 500-ms accumulation time. The duration of an A-scan was thus 350 sec.

The sample was then moved to the next transverse position, with a step size of 5 $\mu$m in the $x$ direction, and the next A-scan was recorded. The step size was chosen to be 5 $\mu$m since the transverse resolution of the imaging system was estimated to be $\approx 10\,\mu$m, based on a collimated beam width of $\approx 2.5$ mm, a focal length of $\approx 25$ mm for lens L5, and the central wavelength of 1064nm. The sample was scanned in the $x$ direction over a range of 800 $\mu$m, so that 160 scans were collected in the axial direction. The limited photon flux available from the downconversion source and the limited quantum efficiency (5–12%) of the particular SSPDs that we used in these experiments [10] result in long acquisition times. These can be decreased, however, by making use of a more powerful laser pump, a chirped SPDC structure with higher conversion efficiency, optics that is optimized over a broad wavelength band, and a detector with higher quantum efficiency.

The collected A-scans were used to construct an $xz$ B-scan of the onion-skin sample using broadband SPDC (from the structure with the greatest chirp at a temperature of 80° C; see Sec. 3.B) in conjunction with a SSPD. The results are illustrated in Fig. 6(a). The two surfaces of several onion-skin cells are apparent (the size of an individual cell falls in the range of onion-skin cells observed using other imaging modalities; see, for example, Figs. 2(c), 4, and 6 of Ref. [19]). We also constructed a B-scan of the same sample with the SPDC source replaced by a standard SLD (see Sec. 3.B), again using the SSPD. The results are displayed in Fig. 6(b). It is apparent that the resolution is diminished when the SPDC source is replaced by a SLD, by virtue of the narrower bandwidth of the latter.

These results confirm once again that, in the vicinity of 1064 nm, and of the source/detector combinations examined, the best resolution was obtained by using broadband downconverted light and a superconducting detector.

## 4. Discussion

Coherence-domain imaging systems can be operated in a single-photon counting mode, offering low detector noise; this in turn leads to increased sensitivity for weak light sources and weakly reflecting samples [10]. In this paper, we have demonstrated that excellent axial resolution can be obtained in a photon-counting coherence-domain imaging system that uses light generated via spontaneous parametric down-conversion (SPDC) in a chirped periodically poled stoichiometric lithium tantalate (chirped-PPSLT) structure, in conjunction with

a niobium nitride superconducting single-photon detector (SSPD).

The bandwidth of the light generated via SPDC, as well as the bandwidth over which the SSPD is sensitive, can extend over a wavelength region that stretches from 700 to 1500 nm. This ultra-broad wavelength band offers a near-ideal combination of deep penetration and ultra-high axial resolution for the imaging of biological tissue.

The generation of SPDC light of adjustable bandwidth in the vicinity of 1064 nm, via the use of chirped-PPSLT structures, has not been achieved previously. Unlike many other broadband sources, the spectra are stable and predictable. We also showed that the observed spectral characteristics of this source accord well with those calculated based on a second-order nonlinear-optics model, indicating that we have the capability of engineering broadband near-infrared sources as desired.

There are a number of limitations associated with this system, however: (1) the SPDC source is more complex and expensive than commonly used SLDs; (2) SPDC generates substantially lower optical photon flux than other commonly used broadband sources, such as SLDs, fsec lasers, fiber lasers [20], and supercontinuum sources generated by photonic-crystal fibers [21], resulting in long data-acquisition times; and (3) the use of SSPDs is complicated by their small active areas and low quantum efficiencies, as well as by the need for cryogenic operation.

Nevertheless, in the vicinity of 1064 nm, we have explicitly demonstrated that the axial resolution offered by the SPDC/SSPD source/detector combination exceeds that achievable with either a superluminescent diode (SLD) as the source, or a single-photon avalanche detector (SPAD) as the detector. These findings were confirmed by the coherence-domain imaging of a hierarchy of samples of increasing complexity: a mirror, a nitrocellulose membrane, and a biological sample comprising onion-skin cells.

## 5. Acknowledgments

This work was supported by the Bernard M. Gordon Center for Subsurface Sensing and Imaging Systems (CenSSIS), an NSF Engineering Research Center, and by a U.S. Army Research Office (ARO) Multidisciplinary University Research Initiative (MURI) Grant.

## References

1. B. E. A. Saleh and M. C. Teich, *Fundamentals of Photonics*, 2nd ed. (Wiley, Hoboken, NJ, 2007), Secs. 11.2B, 21.2E, and 24.5.
2. M. E. Brezinski, *Optical Coherence Tomography: Principles and Applications* (Academic Press, San Diego, 2006).
3. A. F. Fercher, W. Drexler, C. K. Hitzenberger, and T. Lasser, "Optical coherence tomography—principles and applications," Rep. Prog. Phys. **66**, 239–303 (2003).

4. S. A. Boppart, B. E. Bouma, C. Pitris, J. F. Southern, M. E. Brezinski, and J. G. Fujimoto, "*In vivo* cellular optical coherence tomography imaging," Nat. Med. **4**, 861–865 (1998).
5. M. R. Hee, J. A. Izatt, E. A. Swanson, D. Huang, J. S. Schuman, C. P. Lin, C. A. Puliafito, and J. G. Fujimoto, "Optical coherence tomography of the human retina," Arch. Ophthalmol. **113**, 325–332 (1995).
6. J. Welzel, "Optical coherence tomography in dermatology: A review," Skin Res. and Technol. **7**, 1–9 (2001).
7. G. J. Tearney, H. Yabushita, S. L. Houser, H. T. Aretz, I. K. Jang, K. Schlendorf, C. R. Kauffman, M. Shishkov, E. F. Halpern, and B. E. Bouma, "Quantification of macrophage content in atherosclerotic plaques by optical coherence tomography," Circulation **106**, 113–119 (2003).
8. S. H. Yun, G. J. Tearney, B. J. Vakoc, M. Shishkov, W. Y. Oh, A. E. Desjardins, M. J. Suter, R. C. Chan, J. A. Evans, I.-K. Jang, N. S. Nishioka, J. F. de Boer, and B. E. Bouma, "Comprehensive volumetric optical microscopy *in-vivo*," Nat. Med. **12**, 1429–1433 (2006).
9. W. Drexler, "Ultra-high resolution optical coherence tomography," J. Biomed. Opt. **9**, 47–74 (2004).
10. N. Mohan, O. Minaeva, G. N. Goltsman, M. B. Nasr, B. E. A. Saleh, A. V. Sergienko, and M. C. Teich, "Photon-counting optical coherence-domain reflectometry using superconducting single-photon detectors," Opt. Express **16**, 18118–18130 (2008).
11. S. Carrasco, M. B. Nasr, A. V. Sergienko, B. E. A. Saleh, M. C. Teich, J. P. Torres, and L. Torner, "Broadband light generation by noncollinear parametric downconversion," Opt. Lett. **31**, 253–255 (2006).
12. S. E. Harris, "Chirp and compress: Toward single-cycle biphotons," Phys. Rev. Lett. **98**, 063602 (2007).
13. M. B. Nasr, S. Carrasco, B. E. A. Saleh, A. V. Sergienko, M. C. Teich, J. P. Torres, L. Torner, D. S. Hum, and M. M. Fejer, "Ultrabroadband biphotons generated via chirped quasi-phase-matched optical parametric down-conversion," Phys. Rev. Lett. **100**, 183601 (2008).
14. M. B. Nasr, O. Minaeva, G. N. Goltsman, A. V. Sergienko, B. E. A. Saleh, and M. C. Teich, "Submicron axial resolution in an ultrabroadband two-photon interferometer using superconducting single-photon detectors," Opt. Express **16**, 15104–15108 (2008).
15. A. Bruner, D. Eger, M. B. Oron, P. Blau, M. Katz, and S. Ruschin, "Temperature-dependent Sellmeier equation for the refractive index of stoichiometric lithium tantalate," Opt. Lett. **28**, 194–196 (2003).
16. G. N. Goltsman, O. Okunev, G. Chulkova, A. Lipatov, A. Semenov, K. Smirnov,

B. Voronov, and A. Dzardanov, "Picosecond superconducting single-photon optical detector," Appl. Phys. Lett. **79**, 705–707 (2001).

17. G. N. Goltsman, K. Smirnov, P. Kouminov, B. Voronov, N. Kaurova, V. Drakinsky, J. Zhang, A. Verevkin, and R. Sobolewski, "Fabrication of nanostructured superconducting single-photon detectors," IEEE Trans. Appl. Supercond. **13**, 192–195 (2003).
18. G. N. Goltsman, A. Korneev, I. Rubtsova, I. Milostnaya, G. Chulkova, O. Minaeva, K. Smirnov, B. Voronov, W. Slysz, A. Pearlman, A. Verevkin, and R. Sobolewski, "Ultrafast superconducting single-photon detectors for near-infrared-wavelength quantum communications," Phys. Status Solidi C **2**, 1480–1488 (2005).
19. M. B. Nasr, D. P. Goode, N. Nguyen, G. Rong, L. Yang, B. M. Reinhard, B. E. A. Saleh, and M. C. Teich, "Quantum optical coherence tomography of a biological sample," Opt. Commun. **282**, 1154–1159 (2009).
20. H. Lim, Y. Jiang, Y. Wang, Y. Huang, Z. Chen, and F. W. Wise, "Ultrahigh-resolution optical coherence tomography with a fiber laser source at 1 $\mu$m," Opt. Lett. **30**, 1171–1173 (2005).
21. B. Povazay, K. Bizheva, A. Unterhuber, B. Hermann, H. Sattmann, A. F. Fercher, W. Drexler, A. Apolonski, W. J. Wadsworth, J. C. Knight, P. St. J. Russell, M. Vetterlein, and E. Scherzer, "Submicrometer axial resolution optical coherence tomography," Opt. Lett. **27**, 1800–1802 (2002).

**List of Figure Captions**

Fig. 1. Brightness images, in which brightness is proportional to the calculated power spectral density of the emission, at various temperatures. The features of the structures are specified by the length of the first period $b_1$ and the chirp parameter $\zeta$. (a) Unchirped structure with $b_1 = 7.95\,\mu$m and $\zeta = 0$. (b) Medium-chirped structure with $b_1 = 7.85\,\mu$m and $\zeta = 1.26 \times 10^{-6}\ \mu\text{m}^{-1}$. (c) Maximum-chirped structure with $b_1 = 7.5\,\mu$m and $\zeta = 6.24 \times 10^{-6}\ \mu\text{m}^{-1}$. (d) Calculated normalized spectrum for the maximum-chirped structure at a temperature of 80° C. The parameters were chosen to match those of the structures used in the experiments described subsequently. The bandwidth increases substantially with the chirp parameter.

Fig. 2. (a) The generic experimental arrangement makes use of a Michelson interferometer comprising a beam-splitter (BS), reference mirror, and sample. The broadband light emanating from the source is coupled into a SM fiber and collimated by lens L3. The light within the interferometer is focused onto the reference mirror and the sample using lenses L4 and L5, respectively. The lenses, reference mirror, and sample are placed on nanopositioning stages to change their positions, as indicated by the arrows. Experiments were performed using both SSPDs and SPADs as detectors. (b) The downconversion source consists of light from a cw frequency-doubled $Nd^{3+}$:$YVO_4$ laser (Coherent Verdi), operating at a wavelength of 532 nm and at a power of 2 W, that pumps a chirped-PPSLT device. The structure is aligned to obtain collinear SPDC. The downconverted light is collimated using lens L1 and coupled into a SM fiber via lens L2. The filter removes the pump light and allows only the downconverted light to be coupled into the fiber.

Fig. 3. Brightness images, in which brightness is proportional to the measured power spectral density of the emission, at various temperatures, from: (a) the unchirped structure; (b) the medium-chirped structure; and (c) the maximum-chirped structure. (d) Measured normalized spectrum for light from the maximum-chirped structure at a temperature of 80° C. The results bear considerable resemblance to the calculations displayed in Fig. 1.

Fig. 4. Normalized interferograms and their envelopes vs. reference-arm displacement for a mirror sample (A-scans). In all cases, the step size used in constructing the interferograms was 100 nm and the duration of the counting-time windows was 300 ms. (a) Downconversion/superconducting-detector (SPDC/SSPD). The FWHM of the interferogram envelope was 1.6 $\mu$m. The highest resolution was achieved with this combination. (b) Downconversion/avalanche-detector (SPDC/SPAD). The FWHM of the interferogram envelope was 2.8 $\mu$m. (c) Superluminescence/superconducting-detector (SLD/SSPD). The

FWHM of the interferogram envelope was 6.3 $\mu$m.

Fig. 5. Normalized interferograms vs. reference-arm displacement for a pellicle sample (A-scans). In all cases, the step size used in constructing the interferograms was 100 nm and the duration of the counting-time windows was 300 ms. (a) Downconversion/superconducting-detector (SPDC/SSPD). This combination permitted reflections from the two surfaces to be resolved. (b) Downconversion/avalanche-detector (SPDC/SPAD). The two surfaces were not resolved. (c) Superluminescence/superconducting-detector (SLD/SSPD). The two surfaces were not resolved.

Fig. 6. Two-dimensional ($xz$) B-scans of an onion-skin sample. (a) Scan collected using broadband downconversion light and a superconducting detector (SPDC/SSPD). (b) Scan collected from the same onion-skin sample using superluminescence light and the same superconducting detector (SLD/SSPD). Higher axial resolution is attained by using downconversion, by virtue of its broader bandwidth. These cross-sectional views of the tissue highlight the relatively large reflectances at cellular surfaces, which stem from refractive-index discontinuities.

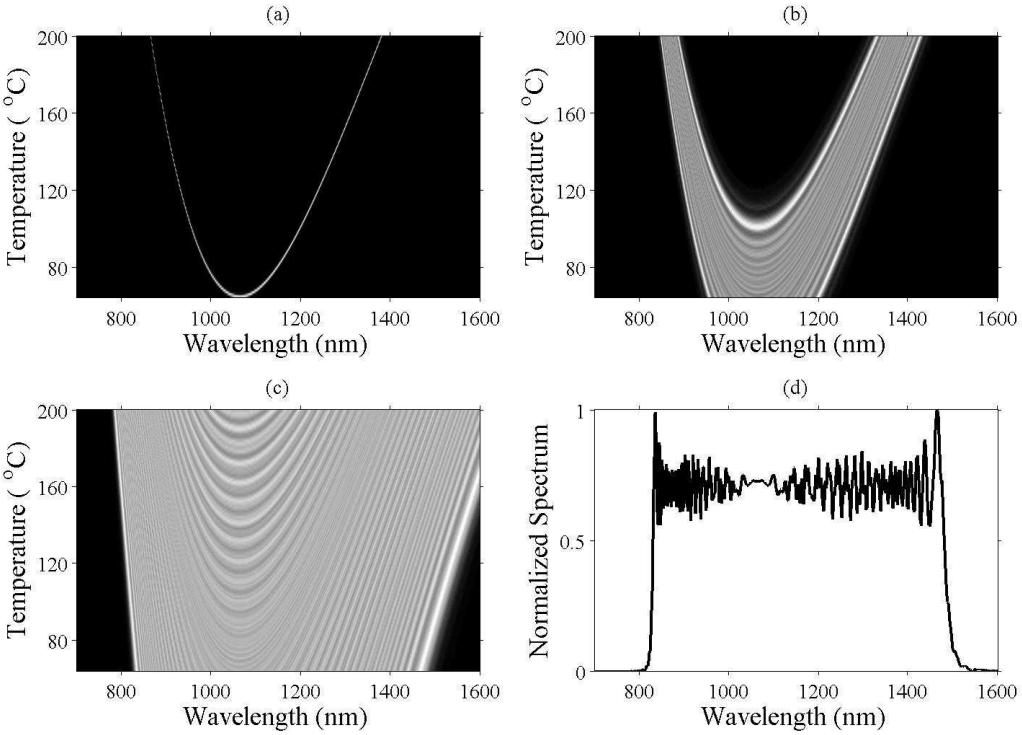


Figure 1. Brightness images, in which brightness is proportional to the calculated power spectral density of the emission, at various temperatures. The features of the structures are specified by the length of the first period $b_1$ and the chirp parameter $\zeta$. (a) Unchirped structure with $b_1 = 7.95\,\mu$m and $\zeta = 0$. (b) Medium-chirped structure with $b_1 = 7.85\,\mu$m and $\zeta = 1.26 \times 10^{-6}\,\mu\text{m}^{-1}$. (c) Maximum-chirped structure with $b_1 = 7.5\,\mu$m and $\zeta = 6.24 \times 10^{-6}\,\mu\text{m}^{-1}$. (d) Calculated normalized spectrum for the maximum-chirped structure at a temperature of 80° C. The parameters were chosen to match those of the structures used in the experiments described subsequently. The bandwidth increases substantially with the chirp parameter. Simulations-f1.eps.

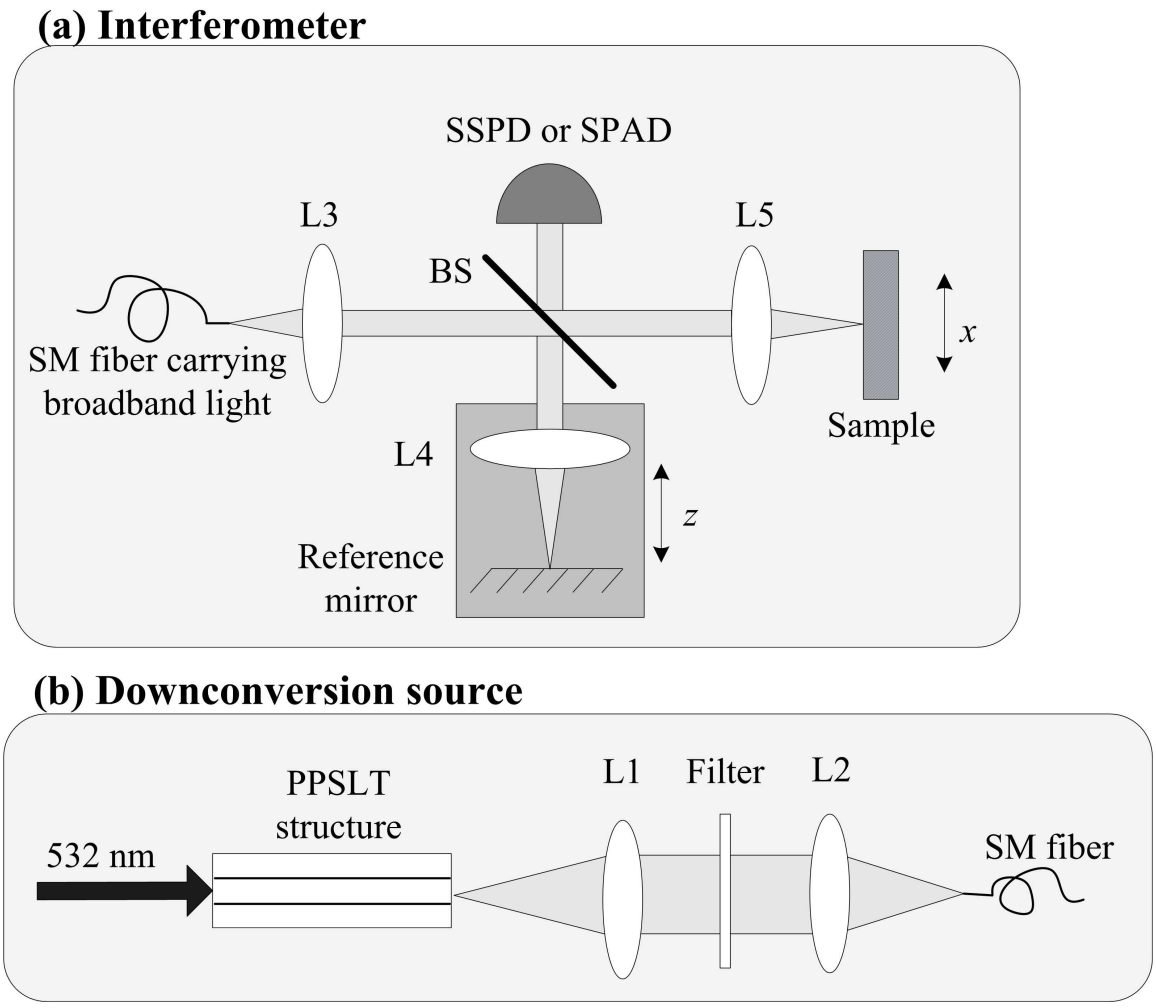


Figure 2. (a) The generic experimental arrangement makes use of a Michelson interferometer comprising a beam-splitter (BS), reference mirror, and sample. The broadband light emanating from the source is coupled into a SM fiber and collimated by lens L3. The light within the interferometer is focused onto the reference mirror and the sample using lenses L4 and L5, respectively. The lenses, reference mirror, and sample are placed on nanopositioning stages to change their positions, as indicated by the arrows. Experiments were performed using both SSPDs and SPADs as detectors. (b) The downconversion source consists of light from a cw frequency-doubled $Nd^{3+}$:$YVO_4$ laser (Coherent Verdi), operating at a wavelength of 532 nm and at a power of 2 W, that pumps a chirped-PPSLT device. The structure is aligned to obtain collinear SPDC. The downconverted light is collimated using lens L1 and coupled into a SM fiber via lens L2. The filter removes the pump light and allows only the downconverted light to be coupled into the fiber. PPSLTSource-f2.eps.

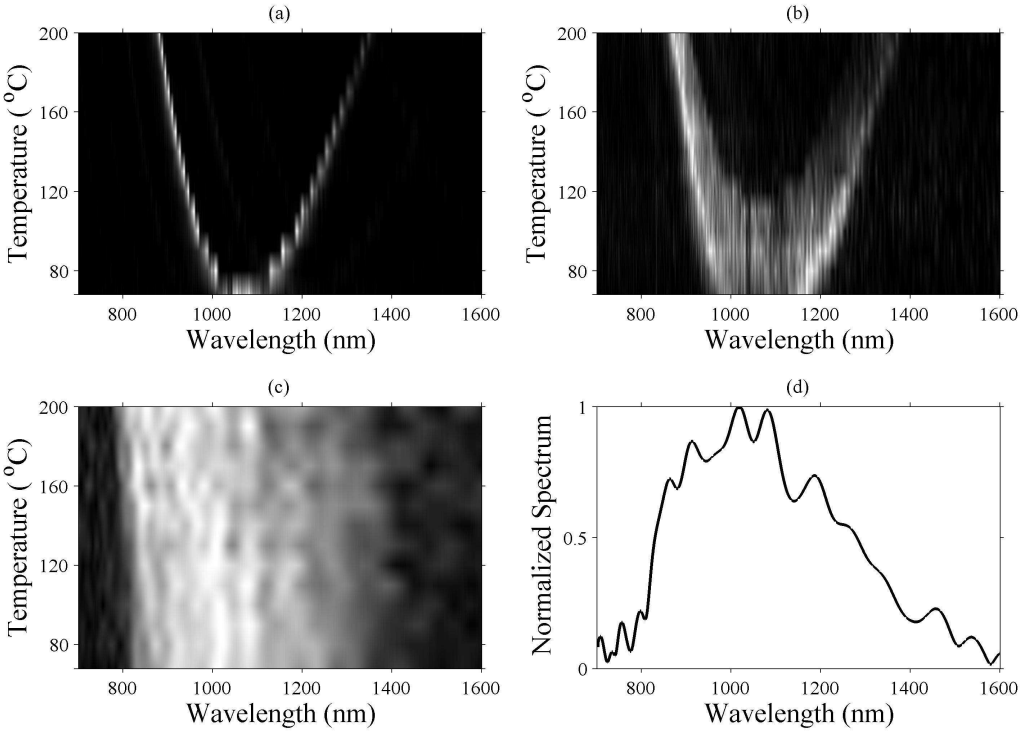


Figure 3. Brightness images, in which brightness is proportional to the measured power spectral density of the emission, at various temperatures, from: (a) the unchirped structure; (b) the medium-chirped structure; and (c) the maximum-chirped structure. (d) Measured normalized spectrum for light from the maximum-chirped structure at a temperature of 80° C. The results bear considerable resemblance to the calculations displayed in Fig. 1. ExperimentalSpectra-f3.eps.

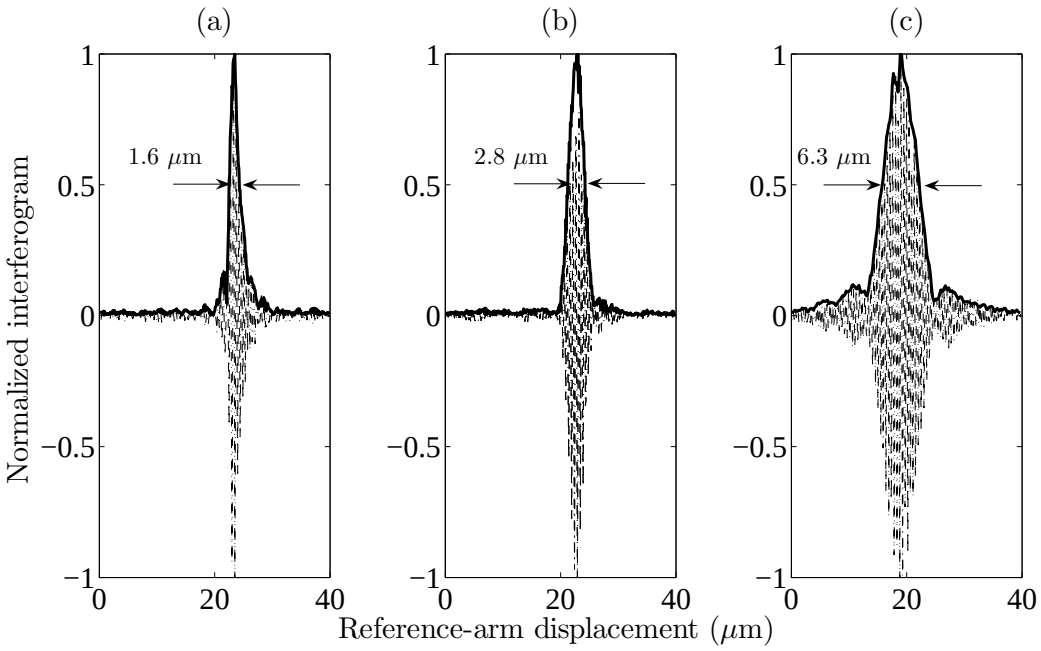


Figure 4. Normalized interferograms and their envelopes vs. reference-arm displacement for a mirror sample (A-scans). In all cases, the step size used in constructing the interferograms was 100 nm and the duration of the counting-time windows was 300 ms. (a) Downconversion/superconducting-detector (SPDC/SSPD). The FWHM of the interferogram envelope was 1.6 $\mu$m. The highest resolution was achieved with this combination. (b) Downconversion/avalanche-detector (SPDC/SPAD). The FWHM of the interferogram envelope was 2.8 $\mu$m. (c) Superluminescence/superconducting-detector (SLD/SSPD). The FWHM of the interferogram envelope was 6.3 $\mu$m. Resolution-f4.eps.

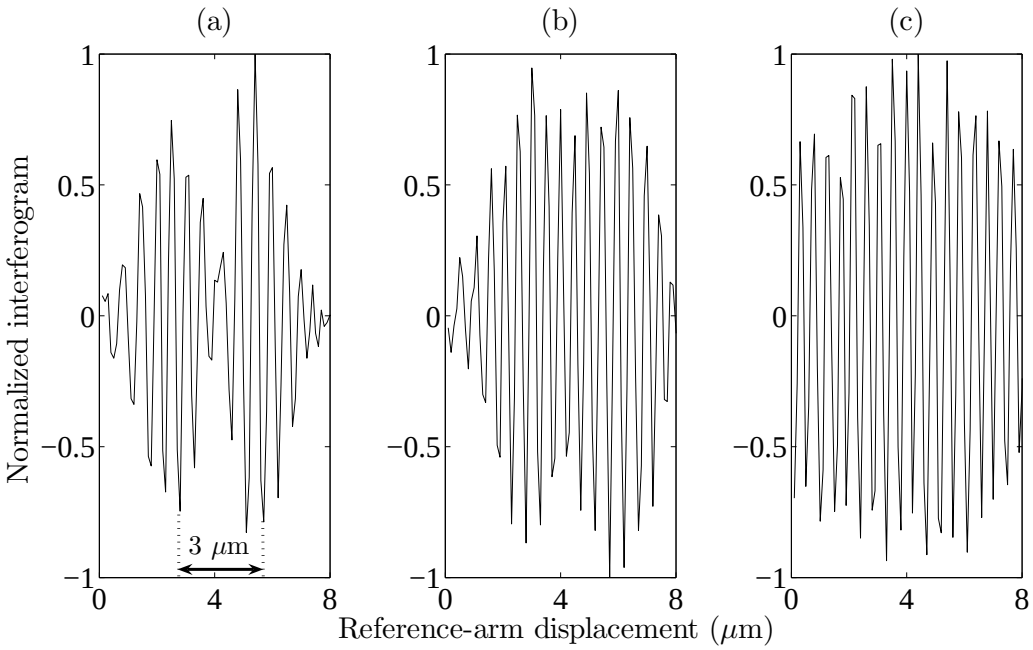


Figure 5. Normalized interferograms vs. reference-arm displacement for a pellicle sample (A-scans). In all cases, the step size used in constructing the interferograms was 100 nm and the duration of the counting-time windows was 300 ms. (a) Downconversion/superconducting-detector (SPDC/SSPD). This combination permitted reflections from the two surfaces to be resolved. (b) Downconversion/avalanche-detector (SPDC/SPAD). The two surfaces were not resolved. (c) Superluminescence/superconducting-detector (SLD/SSPD). The two surfaces were not resolved. Pellicle-f5.eps.

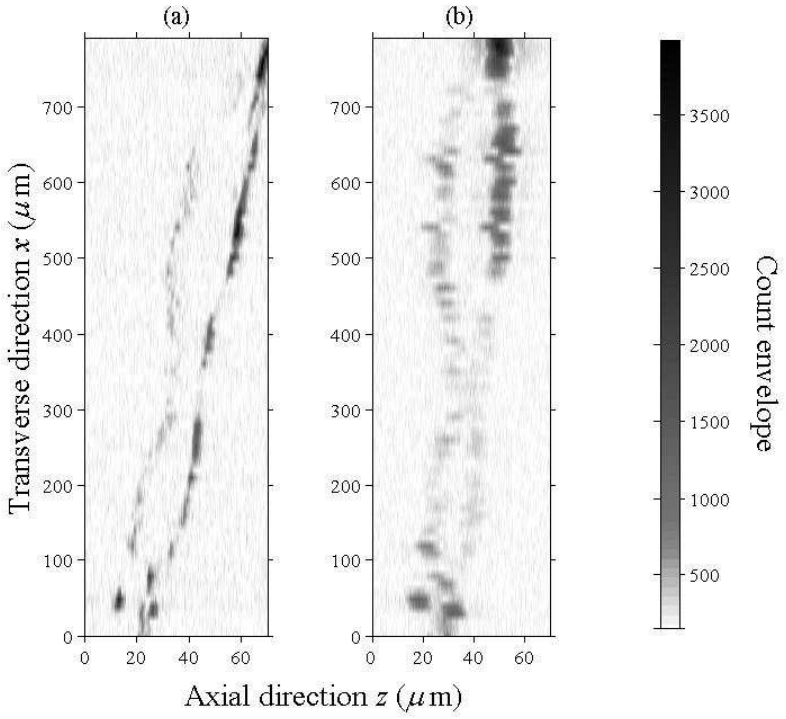


Figure 6. Two-dimensional ($xz$) B-scans of an onion-skin sample. (a) Scan collected using broadband downconversion light and a superconducting detector (SPDC/SSPD). (b) Scan collected from the same onion-skin sample using superluminescence light and the same superconducting detector (SLD/SSPD). Higher axial resolution is attained by using downconversion, by virtue of its broader bandwidth. These cross-sectional views of the tissue highlight the relatively large reflectances at cellular surfaces, which stem from refractive-index discontinuities. Onion-f6.eps.